Journal of the American Ceramic Society
Volume 99, Issue 1, January 2016, pp. 20-26
DOI:10.1111/jace.13869

Influence of process parameters on the morphology of spray-dried $BaCl_2$ powders

W. Taylor Shoulders[1,*], Gregory Bizarri[3], Edith Bourret[3], Romain M. Gaume[1,2]

[1]CREOL, The College of Optics and Photonics at the University of Central Florida, Orlando, FL 32816
[2]NanoScience Technology Center, at the University of Central Florida, Orlando, FL 32816
[3]Lawrence Berkeley National Laboratory, 1 Cyclotron Road, Berkeley, CA 9472

Spray-drying is an effective method for producing powder aggregates with controlled size and morphology. Here, we report on a systematic study aimed at determining how spray-drying parameters such as nozzle temperature, gas flow, salt concentration and solution feed rate, influence the characteristics of $BaCl_2$ granules prepared from aqueous solutions. We correlate the granule characteristics to these conditions through the use of processing maps and modeling. It is found that well-dispersed, high density and spherical aggregates, which are favorable for subsequent powder compaction and sintering, can be obtained within a limited range of processing conditions.

I. Introduction

Controlling powder characteristics such as particle size, size distribution, morphology, agglomeration rate, bulk density and moisture content is essential to many aspects of ceramic processing[1]. In particular, spherical particles provide good packing density and lead to higher sintered density[2]. To this end, the technique of spray-drying, which allows the continuous production of dry granulated powders from an aerosol phase, is one of the most widely used techniques in the industry because of its ability to control these characteristics accurately[3, 4]. The aerosol is either made of fine droplets of dispersions (slurry) or

* tshoulders@knights.ucf.edu

solutions, which undergo controlled evaporation by contact with a warm carrier gas in a drying chamber. The drying conditions (air flow, temperature, and partial pressure of solvent) as well as the characteristics of the aerosol (droplet size, temperature and the mass fraction of solid or solute) determine the morphology of the particles that are produced. Spray-dried particles are typically spherical and on the order of a few microns in size. It has long been known that elevated drying temperatures, for example, lead to the formation of large particles with low density, while slower drying conditions favor small, compact particles with higher densities. While the ceramic literature abounds with studies devoted to the spray-drying of slurry aerosols such as alumina, yttrium aluminum garnet or zirconia in water and ethanol[5,6], fewer papers report on the spray-drying of solution aerosols[7,8].

The motivation of this work resides in some recently identified, high-brightness inorganic scintillators, used in high energy radiation detection, and for which no satisfying commercial powders are available yet. Such materials, amenable to ceramic processing, include several water-soluble barium compounds such as Eu^{2+}:$BaCl_2$[9,10]. In this paper, we demonstrate the spray-drying of micron-size, spherical and dispersed $BaCl_2$ agglomerates suitable for the fabrication of transparent ceramics. In the course of exploring drying parameters and finding the powders most suitable for sintering, a comprehensive understanding of the effects of process parameters on particle morphology was developed. Both experimental and theoretical arguments are used to explain particle formation during spray-drying.

II. Spray-drying of saline solutions

The basic steps of the spray drying process are: (1) the atomization of the feed solution into droplets, usually through a pneumatic nozzle, (2) the mixing of the droplets with the dry air being circulated through the drying chamber, (3) the evaporation of droplets and (4) the separation of the dried powder from the carrier gas. A wide body of work addresses the process of particle formation during spray-drying. These studies mostly report on single droplet drying experiments conducted in controlled environments[11–14], purely theoretical work including mass and heat transfer calculations for droplets[15–17]

and a combination of experimental and theoretical work on actual multiple-particle spray dryers[18, 19]. Many factors affect the final morphology of the particles, but most published theories focus on the drying mechanism in single droplets under controlled conditions. The following is a summary of the initial stages of drying described by many models and reviewed in the comprehensive article by Mezhericher *et. al*[20]. It only takes milliseconds for the droplet to reach thermal equilibrium with the drying air and begin evaporating at a constant rate. This stage proceeds as long as the surface remains saturated with liquid. If the evaporation proceeds too quickly for the solute to redistribute by diffusion in the liquid droplet, then a solid crust forms. The low permeability of this crust may affect further drying by impeding the evaporation of the solvent trapped in the center. Depending on the nature of the surface layer, several pathways are possible. The temperature of the droplet may increase because of hindered mass transport in the droplet subsurface. This may result in an increase in pressure when the temperature exceeds the boiling point of the solvent. Under these conditions, the shell may either swell or fracture and a wide variety of particles shapes can be produced through this process. If the crust is porous and allows for the outward percolation of water, then a solid egg-shell can form. It is however possible to obtain dense granules under a particular set of conditions described by Jayanthi *et al.*[21]. This can be understood by considering the slope of the radial concentration profile of the solute in the droplet. Steep concentration profiles at the point of critical supersaturation lead to crust formation before any precipitate forms near the center of the droplet, whereas flatter concentration profiles lead to volume precipitation and dense particles. The development of a specific concentration profile depends heavily on the radial temperature profile as well as on the initial concentration of solute in the droplet. Other factors also affect the formation of irregular particles: if droplets exit the nozzle with a high Reynolds number, their shape oscillates before stable drops are formed. Under high evaporation rate, unstable droplets lead to non-spherical, porous, plate-like or spherulitic aggregates unsuitable for compaction. Similarly, the coalescence of incompletely dried droplets will produce hard agglomerates of smaller aggregates. Some of these aspects are discussed in the experimental work by Lin *et al.*[12] on the influence of processing conditions on the morphology of various water-soluble salts including calcium acetate, sodium chloride,

ammonium chloride. These past studies provide a useful basis for the systematic study of the effect of spray drying parameters on the morphology of $BaCl_2$ powders.

III. Experimental Procedure

1. Material

$BaCl_2$ can crystallize in the anhydrous, mono-hydrate, or di-hydrate form depending on the partial pressure of water. The transition from one phase to the other is a reversible process[22, 23]. Three aqueous solutions of varied $BaCl_2$ concentrations were prepared by dissolving an appropriate mass of barium chloride di-hydrate $BaCl_2 \bullet 2H_2O$ (99.9% purity, Alfa Aesar) into deionized water. The concentration of these solutions with respect to the solubility limit of anhydrous $BaCl_2$ in water is show on Fig. 1. This study focuses only on the 8.66g/100mL concentration as it produced free-flowing spherical powders as well as a wide range of other morphologies if we deviated from ideal processing conditions.

2. Spray dryer

Our experiments were carried out with a tabletop spray-dryer (Büchi B-290) fitted with the inert loop cooling module (Büchi B-295) set at 17°C. The spray dryer was operated in a closed loop mode, where high purity nitrogen working gas exiting the cyclone was fed into the cooling loop, heated and accelerated back into the drying chamber by the aspirator. To ensure maximum separation rate in the cyclone, the aspirator, which determines the velocity of the gas moving through the system, was set at its maximum capacity (38 m^3/hr). The spray nozzle has a 0.7-mm opening for the feed solution and a 1.4-mm diameter opening for the gas in the two-fluid geometry. The feed solution of $BaCl_2$ was introduced into the nozzle using a peristaltic pump. Four independent experimental parameters were explored in this study: (1) the solution feed rate, (2) the atomization gas flow and (3) the drying gas inlet temperature. Each of these

parameters was varied over a range of values (low, medium and high) as presented in Table 1. A total of 27 separate powder samples, about 2 g each, were produced and subsequently characterized.

3. *Characterization of powders*

The morphology of the powders collected from each experiment was examined by scanning electron microscopy (SEM, Zeiss Ultra-55). The particle size distribution was measured with an acoustic particle size analyzer (AZR-2X, Colloidal Dynamics). For the AZR-2X measurement, powder samples were dispersed into 1,2 dichloroethane using 1% solid loading fraction and dioctyl sodium sulfosuccinate (AOT) as a dispersant. Particle morphology was examined by SEM both before and after preparation of the slurry to confirm that $BaCl_2$ has negligible solubility in dichloroethane. Size distribution was determined by an average of three measurements using the ESA method[24]. The distribution is assumed to be lognormal with the range and center of the distribution being fitting parameters. A statistical analysis of particle sizes in SEM micrographs is used to supplement the particle size data from the AZR-2X. The diameters of 40 particles across 2 SEM micrographs with different magnifications were measured using the ImageJ[25] software measurement tool calibrated to the scale bar produced by Zeiss software. A histogram of particle size versus population was constructed using a bin size of $10^{0.33x}$, where x is an integer, in order to correlate well to the log scale of the AZR-2X. Powder x-ray diffraction (XRD) was performed in the Bragg-Brentano geometry (Rigaku D/Max) using copper-Kα radiation to determine the phase of the powders. Loose powders were pressed lightly into an aluminum sample holder for measurement.

IV. Results and Discussion

The examination of powder samples by SEM reveals that, compared to the irregular raw commercial powders, the morphology of spray-dried powders fall into five different categories depending on the

processing conditions: 1) platelet aggregates, 2) hard agglomerates of spherical granules, 3) spherulites, 4) hollow shells, and 5) dispersed, denser, spherical aggregates, all of which are shown in Fig. 2. The typical size distribution of dispersed, dense aggregate powders is shown in Fig. 3. The lognormal distribution obtained by AZR-2X measurements is centered around 0.7 μm with a range of 0.1 μm to 7 μm. This distribution is more symmetric and has a slightly lower mean particle size compared to the histogram obtained from SEM micrographs of the same powder sample. The slight discrepancy is likely a combination of the small sample size in the SEM size analysis and the imperfect properties of the suspension. These SEM micrographs also show spherical aggregates are composed of elongated crystallites with an average length below 500 nm. Comparison of XRD patterns collected from both commercial and spray dried powders with patterns from literature reveal the presence of different phases depending on processing conditions[26,27]. Fig. 4a shows the coincidence of the 4 strong peaks between 20^o and 25^o 2θ for the commercial anhydrous powder with those of the anhydrous reference pattern (f). Fig. 4b shows three strong peaks between 20^o and 25^o 2θ for the 130 ^{o}C, 52 l/h, 16.5 ml/min spray-dried powder. These peaks align with those of the mono-hydrate reference pattern (e). The di-hydrate reference pattern (d), which is the most stable form at atmospheric conditions, displays no strong diffraction peaks in the range of 20^o and 25^o 2θ. Fig. 4c shows no peaks in this range for the 110 ^{o}C, 21 ml/min, 52 l/h powder sample and corresponds to the di-hydrate reference pattern (d). Finally, the dispersed, higher density, spherical aggregates have demonstrated good sinterability by compaction at a pressure of 300 MPa and temperature of 350^{o}C. Detailed sintering studies will be presented elsewhere.

V. Processing maps

For a given solution feed rate, the predominance domains for the five powder morphologies described above were plotted as a function of the atomization gas flow and gas inlet temperature. In these processing maps, each domain indicates that a given morphology is more prevalent than any other. Despite the repeatability of the process, the statistical nature of this census yields maps in which domain

boundaries are only approximate. Examples of these processing maps are shown in Fig. 5 to 7. The next three sections give a qualitative analysis of these figures.

1. Low solution feed rate

Moving from left to right along the temperature axis of Fig. 5, the particle morphology transitions from higher density particles to hollow spheres. Evaporation rate is expected to increase with inlet temperature, thus upsetting the balance between the evaporation rate and the ability of the solute to redistribute in the droplet. Moving along the y-axis, the gas flow rate increases. In other words, the solution is sprayed into a finer mist with a more turbulent flow. As a result, drying rates increase as the mean droplet size decreases, and it is expected that a similar change of granule morphology will be observed as in the case of temperature increase. However, large populations of shells are not observed at high gas flow rates. The increased velocity and turbulence with which the mist exits the nozzle at higher flow rate seem to dominate the particle formation process. These conditions may cause an increased number of collisions between droplets early in the drying process, leading to coalescence and the formation of hard agglomerates.

The last particle morphology in the 12 ml/min pump map is the spherulite. Attempts have been made to understand the formation of such particles, the consensus being that a high degree of undercooling and deviation from thermal equilibrium at nuclei-solution interfaces is required.[28, 29] Spherulites in this study are always observed at high inlet temperature. According to calculations of Dalmez, the temperature profile within a droplet can be more than 12^{o}C and increases significantly with temperature in the case of spray dried milk[30]. Thus it is not unreasonable to find the conditions for spherulitic crystallization to be met in our experiments.

2. Intermediate solution feed rate

When the pump rate is increased, the spherulite region increases in size, and the hard agglomerate region shifts to the right to make room for a different morphology, platelet aggregates (Fig. 6). The shift and growth of the hard agglomerate region occurs because more solution is introduced into the system, causing water vapor pressure to increase and drying rates to decrease. Collisions between droplets and damp particles are thus more likely. The platelet aggregates can be considered particles with larger primary grain size, which do not favor assembly into spherical aggregates. At higher feed rates and lower temperatures, the drying rate is lower than at any point on the 12 ml/min feed map. The growth of precipitated nuclei may proceed to a greater extent under these conditions.

3. High solution feed rate

The only notable change in the processing map at high solution feed rate (Fig. 7) is the shift of all boundary lines towards higher temperatures. Higher feed rates increase the water partial pressure in the drying chamber, hence slowing down the drying rate. This in turn favors the formation of large crystallites and hard agglomerates. The region for formation of higher density, spherical aggregates is very limited at this flow rate.

VI. Modeling

1. Approach

In order to better understand the experimental conditions that favor the formation of dispersed, dense, spherical aggregates, and explain our experimental maps more quantitatively, we analyzed the balance

between solvent evaporation rate and diffusional mass transport of the solute during the drying process. This approach has been well documented[31–33]. This balance can be written in the form of a dimensionless Peclet number as follows:

$$Pe = \frac{N}{\rho_l L D} \quad (1)$$

where N is the evaporation rate in kg/s, ρ_l is the density of the liquid phase in the droplet (hence N/ ρ is the corresponding volume of the liquid phase lost to the gas phase per unit time), D is the ambipolar ionic diffusivity of $BaCl_2$ in water and L is the characteristic length over which ionic diffusion proceeds, i.e. the radius of the droplet d/2. The evaporation rate is a function of the droplet surface area, A, the temperature difference between the drying gas and droplet surface, T_{gas} - $T_{droplet}$, the latent heat of evaporation for water H, and the heat transfer coefficient h at the gas-droplet interface:

$$N = \frac{hA(T_{gas} - T_{droplet})}{H} \quad (2)$$

To estimate the value of the heat transfer coefficient, one can use the definition of the dimensionless Nusselt heat transfer coefficient, Nu, (Eq. 3) and the Ranz-Marshall (R-M) correlation for combined laminar and turbulent flows in forced convection[34] (Eq. 4):

$$Nu = \frac{hL}{k} \quad (3)$$

$$Nu = 2.0 + 0.6Re^{0.5}Pr^{0.33} \quad (4)$$

with the Reynolds and Prandtl numbers, Re and Pr, given by:

$$Re = \frac{\rho_g v L}{\eta} \quad (5)$$

$$Pr = \frac{\eta C_p}{k} \quad (6)$$

The definition of the Nusselt number involves the thermal conductivity of the droplet, k, and the characteristic length, L, over which the temperature gradient establishes itself at the liquid-vapor interface. It is assumed here that L~d/2. The definition of the Reynolds number involves the hydrodynamic characteristics dimension of the droplet, L~ d, as it moves at relative speed v in the airstream of density ρ_g and dynamic viscosity, η. The Prandtl number for the air flow involves the heat capacity of the gas, C_p, and its thermal conductivity, k. In order to satisfy the R-M relation, the Reynolds and Prandtl numbers must satisfy Re < 200 and Pr < 250, a situation easily fulfilled across the range of operating conditions used experimentally.[14]

The drying gas temperature, T_{gas}, which enters Eq. 2, is assumed to be equal to the inlet temperature (x-axis of the maps) measured just before it enters the drying chamber. The feed solution is partially warmed up as it travels down the nozzle and the droplet temperature, $T_{droplet}$, at the beginning of the drying stage, is estimated through the following energy balance equation between the inlet and the outlet of the drying chamber:

$$Cp_{H_2O,l}T_{i,H_2O} + m_{N_2}Cp_{N_2}T_{i,N_2} = m_{H_2O}Cp_{H_2O,v}T_{o,H_2O} + m_{N_2}Cp_{N_2}T_{o,N_2} + m_{BaCl_2}Cp_{BaCl_2}T_{o,BaCl_2} + H_v m_{H_2O} - H_c m_{BaCl_2} + hA\Delta T_{wall} \quad (7)$$

Eq. 7 establishes the conservation of free energy between the incoming and outgoing phases and includes the heat absorbed in the conversion of liquid water to vapor, the heat released by the crystallization of the salt and the heat lost through the wall of the drying chamber. The variables m, c_p and

T are the masses, heat capacities and temperatures of each phase, and H_v and H_c are the latent heats of vaporization of water and of crystallization of $BaCl_2.nH_2O$, respectively. During the constant-rate evaporation stage, the temperature of the droplets is equal to the wet-bulb temperature and, at the inlet, $T_{droplet}=T_{i,H2O}$. Because of the small concentration of salt chosen for our experiments, the term corresponding to the release of heat due to crystallization, $H_c m_{BaCl2}$, can be neglected compared to the other terms. The heat loss at the outer surface of the drying chamber is assumed to be in steady state. This balance assumes (1) an isobaric and isochoric process in which no work is produced by the system and (2) all liquid water is converted into vapor. This last assumption is validated by calculating the partial pressure of water for 100% transfer of inlet liquid water to the vapor phase at the outlet. Calculated pressures are compared to the equilibrium partial pressures of water at the anhydrous-to-monohydrate and monohydrate-to-dihydrate transitions in Fig. 8. The majority of conditions are expected to produce the mono-hydrate phase with the exception of spherulitic and hollow shell conditions (high temperature and small droplet sizes), which are expected to produce the anhydrous phase. XRD, examples of which are given in fig. 4, confirms that most conditions indeed produce the mono-hydrate phase, with a few samples processed at lower temperatures and lower solution feeds exhibiting a purely di-hydrate phase. The anhydrous phase was not detected in any powder samples, suggesting hydration of powders with exposure to air during handling or inaccurate prediction of humidity. Nevertheless, the predominant phase in the range of conditions surveyed is found to be the mono-hydrate, as predicted in fig. 4.

The final term to be calculated for estimating N from Eq. (2) is the size of droplets (A), which is determined mostly by the nitrogen gas flow through the nozzle (y-axis in maps). The average droplet diameter decreases with increasing gas flow. Various relations between the droplet size and operating conditions have been proposed in the literature for two-fluid type atomizers.[35] These include analytical models for both the arithmetic average droplet size (d_{10}) and the Sauter mean diameter ($d_{3/2}$). $d_{3/2}$ is more commonly found in spray drying literature, so it will be used for the drier modeling.

$$d_{3,2} = \frac{535 \cdot 10^3}{v}\left(\frac{\gamma}{\rho}\right)^{0.5} + 597 \cdot 10^3 \frac{V_s}{V_g}\left(\frac{\eta}{\sqrt{\gamma\rho}}\right)^{0.45} \quad (8)$$

where $d_{3,2}$ is the Sauter mean diameter (SMD) of the droplets in μm; v is the velocity of the air relative to the liquid at the nozzle orifice (m/s); γ, ρ and η are the surface tension (N/m), density (kg/m^3) and viscosity (Pa·s) of the solution; and V_s and V_g are the volumetric flow rates of the solution and gas, respectively (m^3/s). By definition, $d_{3,2}$, is the diameter of a droplet having the same volume-to-surface area ratio as the entire spray, at the nozzle exit. Fig. 9 compares the $d_{3/2}$ calculated from Eq. 8 and using the experimental conditions from this work, to the arithmetic average droplet size (d_{10}) reported by the manufacturer of our spray-dryer[36]. The published d_{10} falls slightly below that calculated from the Kim-Marshall relationship of d_{10} reported in the literature[35]. Plotting the diameters versus 1/v reveals that the analytical models depend on more than v, so the published data should have significant y-error. Finally, $d_{3/2}$ slightly exceeds d_{10} of the droplets as expected.

2. Construction of Peclet maps

The various physical quantities relevant to the problem and needed to solve Eq. (1) through (8) are listed in Table 2. The mass flux of each phase is determined from calibration tables provided by Büchi[37*] for both gas flow driven by the aspirator and solution flow driven by the peristaltic pump. The feed solution calibration values were crosschecked by measuring the volume pumped in one minute, for each setting, using a graduated cylinder.

---

[*] Solution feed in ml/min is given by 0.3P where P is the percentage setting of the pump. The atomization air flow in l/h follows an exponential relationship given by $109.6e^{0.046G}$, where G is the setting on the flow gauge. Finally, the aspirator influence on drying gas flow is tabulated. The flow is a constant 38 m^3/h for our experiments.

Several simplifying assumptions are made with regard to the thermal masses appearing in Eq. 7: the heat capacity and density of the solution are approximated by those of liquid water since only dilute solutions of $BaCl_2$ are used. Similarly, because the thermal mass of the gas introduced by the atomizer in the system is small in comparison to that of the other fluids entering the drying chamber, its contribution to the energy balance is neglected. It is further assumed that the phases at the outlet of the drying chamber are in thermal equilibrium, thus implying that $T_{o,BaCl2} = T_{o,N2} = T_{o,H2O} = T_{o,meas}$, where $T_{o,meas}$ is the outlet temperature recorded by the built-in sensor of the instrument. At steady state, the rate of heat loss through the walls of the vessel is constant and the heat flux carried by conduction through the walls is equal to that removed by convection from the outer walls by the surrounding air. The average temperature of the vessel's outer wall was measured for three different inlet and outlet temperatures and taken to be a linear function of the temperature drop between the inlet and outlet. Hence, solving Eq. 7 for $T_{droplet}$ and using this solution in Eq. 2, allows one to calculate the evaporation rate and the Peclet number as a function of the inlet temperature and gas flow.

The results of these simulations are represented on Fig. 10. We verified that, for the range of parameters explored in this study, Re and Pr are approximately 1.5 and 0.89 respectively, and confirm the applicability of the R-M correlation. The shape of the contour map for the 12 ml/min pump rate in Fig. 10 shows increasing Peclet number both along the x- and y-axes. As per Fig. 5, the semi-circular predominance domain for the higher density, dispersed particles at 12 ml/min feed rate intersects the temperature axis at 140°C and the gas flow axis at 65 l/h. The contour line corresponding to a Peclet number of 0.6 approximates this predominance domain. As expected, lower Peclet number favors the formation of denser, dispersed particles. The quantitative agreement between the calculated and experimental maps validates a posteriori the various assumptions of the model and demonstrates that this approach can be used in the optimization of powder fabrication with controlled morphologies. At the feed rates of 16.5 ml/min and 21 ml/min, the model does not correlate as well to experiments. A possible explanation is that Peclet number predicts trends in particle density without necessarily being correlated to agglomeration and other more complex morphologies. An interesting future study could involve the

comparison of the model to a processing map based purely on particle density, and not more qualitative morphology descriptions.

VII. Conclusion

Dispersed, higher density, spherical aggregates of $BaCl_2$ were produced by spray drying aqueous solutions. Processing maps were constructed to define the processing conditions conducive to specific powder morphologies. Modeling based on mass and heat balance in the spray dryer has provided confirmation of the trends observed experimentally as well as a more generalized view of the process. In particular, the Peclet number can be a powerful tool for predicting the conditions suitable for the formation of well-dispersed, micron-size spherical aggregates. At the 12 ml/min solution feed rate, values of Peclet number less than 0.6 lead to higher density granules, while larger values favor the formation of hollow, aggregated or spherulitic granules.

Acknowledgments

The authors acknowledge the work of Baochi Doan. This work has been supported by the U.S. Department of Energy/NNSA/DNN R&D and carried out at the University of Central Florida and the Lawrence Berkeley National Laboratory, under Contract NO. AC02-05CH11231. This support does not constitute an express or implied endorsement on the part of the Government.

References

[1] A.C. Bravo, L. Longuet, D. Autissier, J.F. Baumard, P. Vissie, and J.L. Longuet, "Influence of the Powder Preparation on the Sintering of Yb-doped Sc2O3 Transparent Ceramics," *Opt. Mater. (Amst).*, **31** [5] 734–739 (2009).

[2] R.K. McGEARY, "Mechanical Packing of Spherical Particles," *J. Am. Ceram. Soc.*, **44** [10] 513–522 (1961).

[3] S.J. Lukasiewicz, "Spray-Drying Ceramic Powders," *J. Am. Ceram. Soc.*, **72** [4] 617–624 (1989).

[4] B.B. Patel, J.K. Patel, and S. Chakraborty, "Review of Patents and Application of Spray Drying in Pharmaceutical, Food and Flavor Industry.," *Recent Pat. Drug Deliv. Formul.*, **8** [1] 63–78 (2014).

[5] M. Serantoni, A. Piancastelli, A.L. Costa, and L. Esposito, "Improvements in the Production of Yb:YAG Transparent Ceramic Materials: Spray Drying Optimisation," *Opt. Mater. (Amst).*, **34** [6] 995–1001 (2012).

[6] X.. Cao, R. Vassen, S. Schwartz, W. Jungen, F. Tietz, and D. Stöever, "Spray-Drying of Ceramics for Plasma-Spray Coating," *J. Eur. Ceram. Soc.*, **20** [14-15] 2433–2439 (2000).

[7] Y. Yamauchi, P. Gupta, K. Sato, N. Fukata, S. Todoroki, S. Inoue, and S. Kishimoto, "Industrial mass-production of mesoporous silica spherical particles by a spray-drying process: investigation of synthetic conditions," *J. Ceram. Soc. Japan*, **117** [1362] 198–202 (2009).

[8] V.N. Daggupati, G.F. Naterer, K.S. Gabriel, R.J. Gravelsins, and Z.L. Wang, "Effects of Atomization Conditions and Flow Rates on Spray Drying for Cupric Chloride Particle Formation," *Int. J. Hydrogen Energy*, **36** [17] 11353–11359 (2011).

[9] Z. Yan, G. Bizarri, and E. Bourret-Courchesne, "Scintillation Properties of Improved 5% Eu2+-doped BaCl2 Single Crystal for X-ray and γ-ray Detection," *Nucl. Instruments Methods Phys. Res. Sect. A*, **698** 7–10 (2013).

[10] D. Singh, "Structure and Optical Properties of High Light Output Halide Scintillators," *Phys. Rev. B*, **82** [15] 155145 (2010).

[11] G. Brenn, T. Wiedemann, D. Rensink, O. Kastner, and A.L. Yarin, "Modeling and Experimental Investigation of the Morphology of Spray Dryed Particles," *Chem. Eng. Technol.*, **24** [11] 1113–1116 (2001).

[12] J.-C. Lin and J.W. Gentry, "Spray Drying Drop Morphology: Experimental Study," *Aerosol Sci. Technol.*, **37** [1] 15–32 (2003).

[13] M.H. Sadafi, I. Jahn, A.B. Stilgoe, and K. Hooman, "Theoretical and Experimental Studies on a Solid containing Water Droplet," *Int. J. Heat Mass Transf.*, **78** 25–33 (2014).

[14] D.H. Charlesworth and W.R. Marshall, "Evaporation from Drops containing Dissolved Solids," *A.I.Ch.E. J.*, **6** [1] 9–23 (1960).

[15] D.E. Oakley, "Spray Dryer Modeling in Theory and Practice," *Dry. Technol.*, **22** [6] 1371–1402 (2004).

[16] M. Eslamian, M. Ahmed, and N. Ashgriz, "Modeling of Solution Droplet Evaporation and Particle Evolution in Droplet-to-Particle Spray Methods," *Dry. Technol.*, **27** [1] 3–13 (2009).

[17] C.S. Handscomb, "Simulating Droplet Drying and Particle Formation in Spray Towers;" King's College, 2008.

[18] W.J. Walker, J.S. Reed, and S.K. Verma, "Influence of Slurry Parameters on the Characteristics of Spray-Dried Granules," *J. Am. Ceram. Soc.*, **82** [7] 1711–1719 (1999).

[19] P. Seydel, J. Blömer, and J. Bertling, "Modeling Particle Formation at Spray Drying Using Population Balances," *Dry. Technol.*, **24** [2] 137–146 (2006).

[20] M. Mezhericher, A. Levy, and I. Borde, "Theoretical Models of Single Droplet Drying Kinetics: A Review," *Dry. Technol.*, **28** [2] 278–293 (2010).

[21] G. V. Jayanthi, S.C. Zhang, and G.L. Messing, "Modeling of Solid Particle Formation During Solution Aerosol Thermolysis: The Evaporation Stage," *Aerosol Sci. Technol.*, **19** [4] 478–490 (1993).

[22] J. Henning, K. Beckenkamp, and H.D. Lutz, "Single-Crystal Raman Studies on the Solid Hydrates MX2-H20 (M = Ba, Sr; X = OH, Br, I)," *Appl. Spectrosc.*, **44** [6] 992–997 (1990).

[23] R.K. Osterheld and P.R. Bloom, "Dehydration Kinetics for Barium Chloride Dihydrate Single Crystals," *J. Phys. Chem.*, **82** [14] (1978).

[24] R.J. Hunter and R.W.O. Brien, "Electroacoustics;" pp. 1–19 in *Encycl. Surf. Colloid Sci.* 2005.

[25] C.A. Schneider, W.S. Rasband, and K.W. Eliceiri, "NIH Image to ImageJ: 25 years of image analysis," *Nat. Methods*, **9** [7] 671–675 (2012).

[26] *Standard X-ray Diffraction Powder Patterns*, v12 ed. US Department of Commerce, National Bureau of Standards, 1975.

[27] H.D. Lutz, W. Buchmeier, and B. Engelen, "Comparative study of the crystal structures of isotypic MX2.H2O, M = Sr, Ba, and X = Cl, Br, I. Bifurcated H bonds in solid hydrates," *Acta Crystallogr. Sect. B Struct. Sci.*, **43** [1] 71–75 (1987).

[28] L. Gránásy, T. Pusztai, G. Tegze, J. Warren, and J. Douglas, "Growth and form of spherulites," *Phys. Rev. E*, **72** [1] 011605 (2005).

[29] N. Goldenfield, "Theory of Spherulitic Crystallization," *J. Cryst. Growth*, **84** 601–608 (1987).

[30] N. Dalmaz, H.O. Ozbelge, A.N. Eraslan, and Y. Uludag, "Heat and Mass Transfer Mechanisms in Drying of a Suspension Droplet: A New Computational Model," *Dry. Technol.*, **25** [2] 391–400 (2007).

[31] R. Vehring, "Pharmaceutical Particle Engineering via Spray Drying," *Pharm. Res.*, **25** [5] 999–1022 (2008).

[32] D. Huang, "Modeling of Particle Formation During Spray Drying;" pp. 26–28 in *Eur. Dry. Conf. 2011*. 2011.

[33] M. Huyesmans and A. Dassargues, "Review of the use of Péclet Numbers to Determine the Relative Importance of Advection and Diffusion in Low Permeability Environments," *Hydrogeology*, 1–20 (2004).

[34] C.T. Crowe, J.D. Schwarzkopf, M. Sommerfeld, and Y. Tsuji, *Multiphase Flows with Droplets and Particles*. CRC Press, 1997.

[35] K. Masters, *Spray Drying*, second edi. John Wiley and Sons, New York, NY, 1976.

[36] C. Arpagaus and H. Schwartzbach, *Scale-up from the Büchi Mini Spray Dryer B-290 to the Niro MOBILE MINOR*. 2008.

[37] *Buchi B-290 Operation Manual, Version G*, 34–35 (n.d.).

[38] M. Atterer, *Gmelin-Handbuch der anorganischen Chemie System-Nummer 30, Barium*. Verl. Chemie, Weinheim/Bergstr., 1960.

[39] R.T. Balmer, *Thermodynamic Tables to Accompany Modern Engineering Thermodynamics*. Academic Press, 2011.

[40] *CRC Handbook of Chemistry and Physics, 93rd Edition*. CRC Press, 2012.

[41] Y.-H. Li and S. Gregory, "Diffusion of Ions in Sea Water and in Deep-Sea Sediments," *Geochemical Cosmochem. Acta.*, **38** 703–714 (1974).

List of Figure Captions

Fig. 1. The solubility of anhydrous $BaCl_2$ in water[38] is reported along with the concentrations of dilute solutions investigated in this work. All concentrations are based on the anhydrous form.

Fig. 2. SEM micrographs show a) platelet aggregate particles, b) hard agglomerates, c) spherulites, d) hollow shells, e) dispersed, higher density, spherical aggregates and f) commercial hydrate powders.

Fig. 3. The particle size distribution of a dispersed, higher density, spherical powder sample corresponding to Fig. 2e is measured by the AZR-2x and scaled to the left hand axis. The population of particle sizes in Fig. 2e and a second higher magnification micrograph are represented in the histogram scaled to the right hand axis.

Fig. 4. The x-ray diffraction patterns of a commercial anhydrous powder sample (a), the 130 ^{o}C, 52 l/h, 16.5 ml/min spray-dried powder sample (b), and the 110 ^{o}C, 21 ml/min, 52 l/h spray-dried powder sample (c) are compared to the di-hydrate[26] (d), mono-hydrate[27] (e), and anhydrous[26] (f) $BaCl_2$ reference patterns.

Fig. 5. A processing map for a concentration of 8.66g/100 ml and a solution feed rate of 12 ml/min shows morphology regions.

Fig. 6. A processing map for a concentration of 8.66g/100 ml and a solution feed rate of 16.5 ml/min shows morphology regions.

Fig. 7. A processing map for a concentration of 8.66g/100 ml and a solution feed rate of 21 ml/min shows morphology regions.

Fig. 8. The water vapor pressure above solid $BaCl_2 \bullet nH_2O$ at the outlet is calculated for a representative set of spray drying samples. The solid line represents equilibrium vapor pressure between the mono-hydrate and di-hydrate phases, while the dotted line represents the equilibrium vapor pressure between the anhydrous and mono-hydrate phases[38].

Fig. 9 The calculated $d_{3,2}$ plotted versus the inverse relative gas-solution velocity is slightly higher than both the arithmetic average droplet size reported in the spray-dryer literature and the arithmetic average droplet size calculated by the Kim-Marshall equation.

Fig. 10. A contour map of Peclet number versus gas inlet temperature and gas flow for a pump rate of 12 ml/min and feed solution concentration of 8.66 g/100 ml shows good agreement with the experimental morphology boundary (grey shaded region) for higher density, dispersed aggregates.

Table 1. Range of processing parameters studied in this work.

	Low	Medium	High
Feed rate (ml/min)	12	16.5	21
Atomization gas flow (l/h)	26	52	104
Gas inlet temperature (^{o}C)	110	130	150

Table 2. Physical constants used in the numerical simulation**.**

Constant	Value	Units	Ref.
$Cp_{H2O,l}$	4.2	$kJ \cdot kg^{-1} \cdot K^{-1}$	39
$Cp_{H2O,v}$	1.9	$kJ \cdot kg^{-1} \cdot K^{-1}$	39
Cp_{N2}	1.05	$kJ \cdot kg^{-1} \cdot K^{-1}$	39
Cp_{BaCl2}	0.639	$kJ \cdot kg^{-1} \cdot K^{-1}$	38
H_v	2260	$kJ \cdot kg^{-1}$	38
H_c	116.2	$kJ \cdot kg^{-1}$	38
ρ_{N2}	1.165	$kg \cdot m^{-3}$	40
η_{N2}	$2.12 \cdot 10^{-5}$	Pa·s	40
σ_{H2O}	0.0589	N/m	40
η_{H2O}	$2.82 \cdot 10^{-4}$	Pa·s	40
k_{N2}	$3.14 \cdot 10^{-2}$	$W \cdot m^{-1} \cdot K^{-1}$	40
D_{Ba}	$3 \cdot 10^{-6} e^{-\frac{20230}{RT}}$	m^2/s	41
D_{Cl}	$4.33 \cdot 10^{-6} e^{-\frac{18980}{RT}}$	m^2/s	41

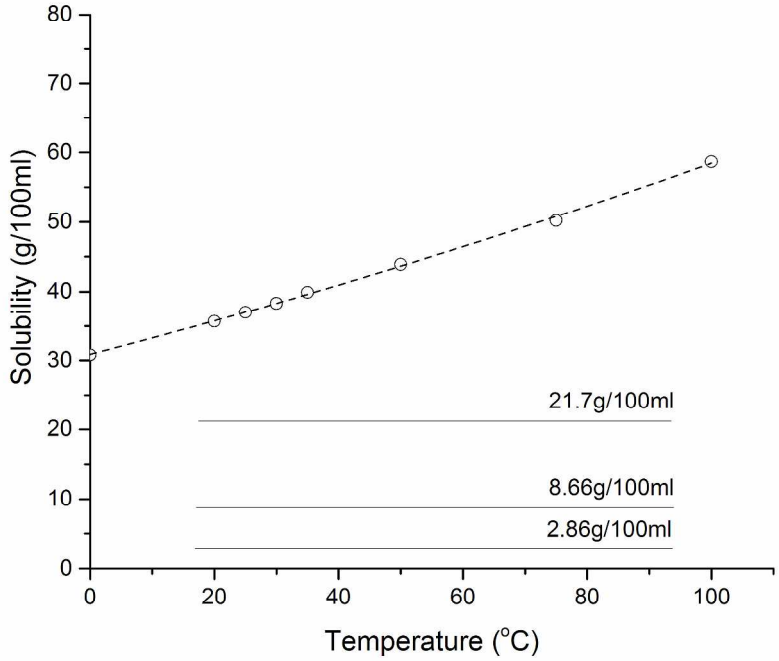

Fig. 1. The solubility of anhydrous BaCl2 in water38 is reported along with the concentrations of dilute solutions investigated in this work. All concentrations are based on the anhydrous form.
279x215mm (300 x 300 DPI)

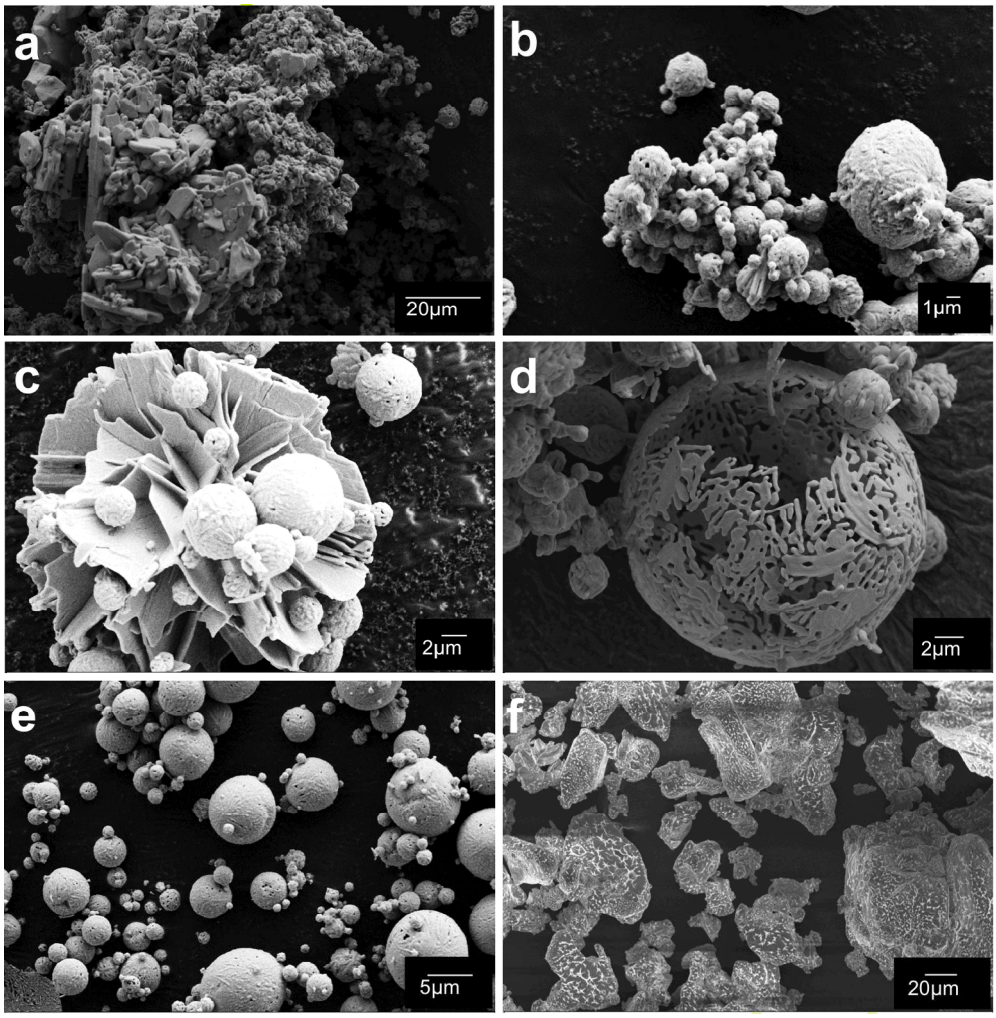

Fig. 2. SEM micrographs show a) platelet aggregate particles, b) hard agglomerates, c) spherulites, d) hollow shells, e) dispersed, higher density, spherical aggregates and f) commercial hydrate powders.
169x170mm (300 x 300 DPI)

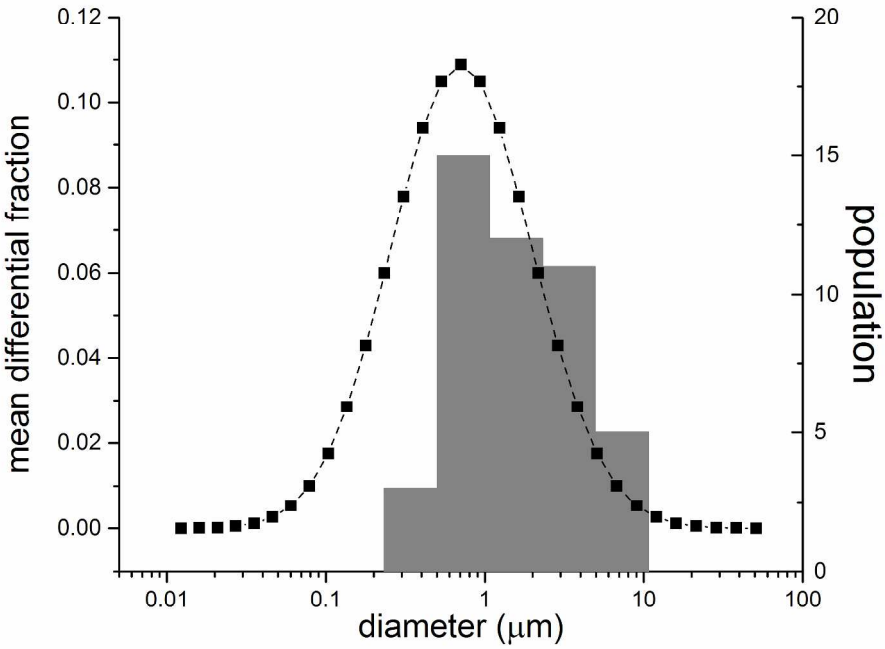

Fig. 3. The particle size distribution of a dispersed, higher density, spherical powder sample corresponding to Fig. 2e is measured by the AZR-2x and scaled to the left hand axis. The population of particle sizes in Fig. 2e and a second higher magnification micrograph are represented in the histogram scaled to the right hand axis.
279x215mm (300 x 300 DPI)

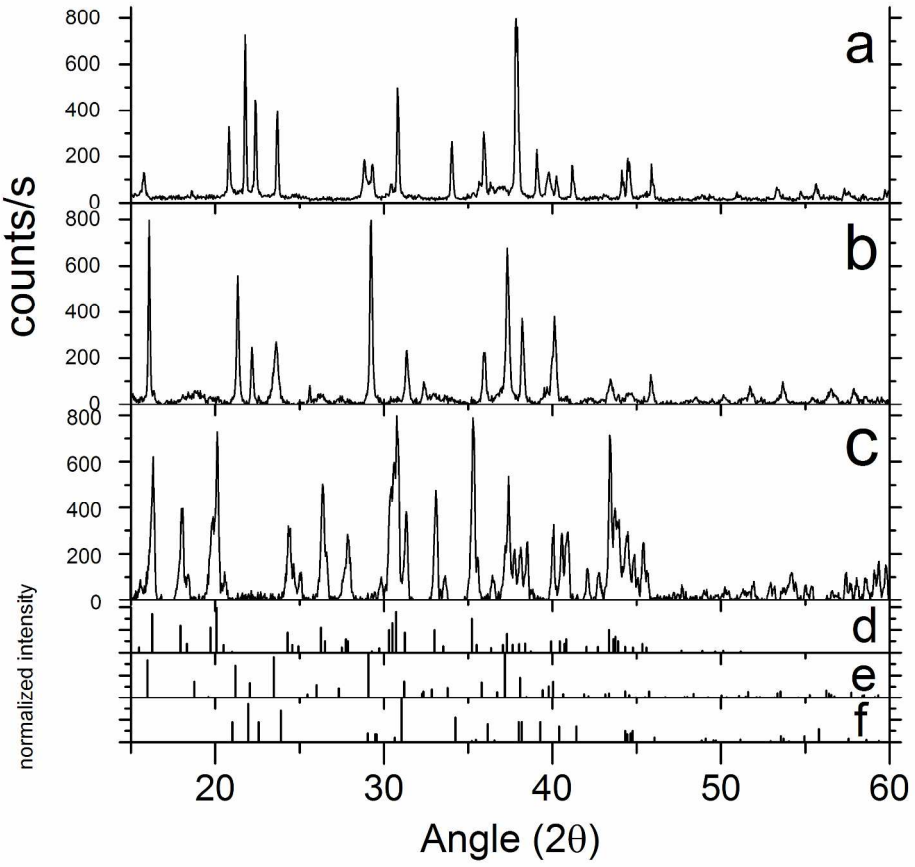

Fig. 4. The x-ray diffraction patterns of a commercial anhydrous powder sample (a), the 130 oC, 52 l/h, 16.5 ml/min spray-dried powder sample (b), and the 110 oC, 21 ml/min, 52 l/h spray-dried powder sample (c) are compared to the di-hydrate26 (d), mono-hydrate27 (e), and anhydrous26 (f) BaCl2 reference patterns.
251x245mm (300 x 300 DPI)

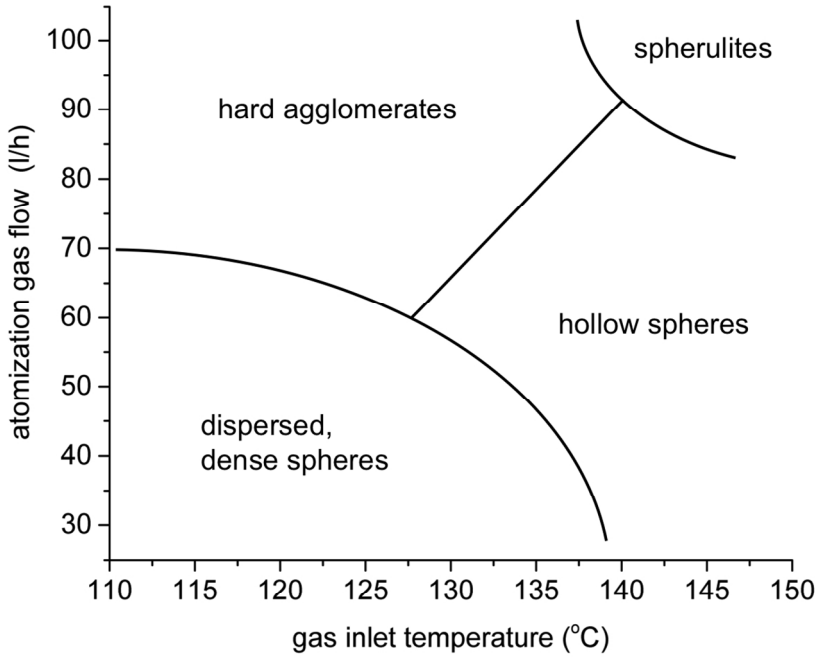

Fig. 5. A processing map for a concentration of 8.66g/100 ml and a solution feed rate of 12 ml/min shows morphology regions.
123x95mm (300 x 300 DPI)

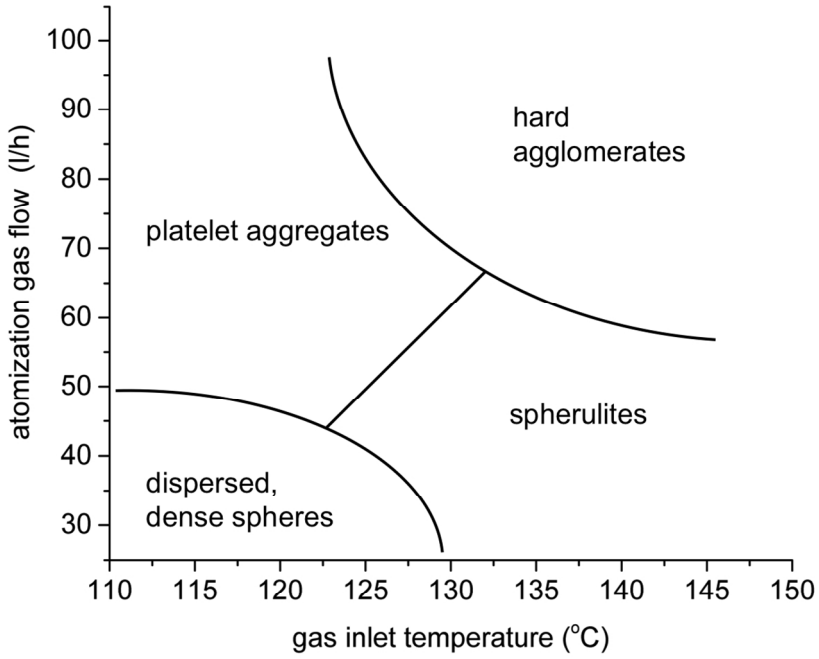

Fig. 6. A processing map for a concentration of 8.66g/100 ml and a solution feed rate of 16.5 ml/min shows morphology regions.
123x95mm (300 x 300 DPI)

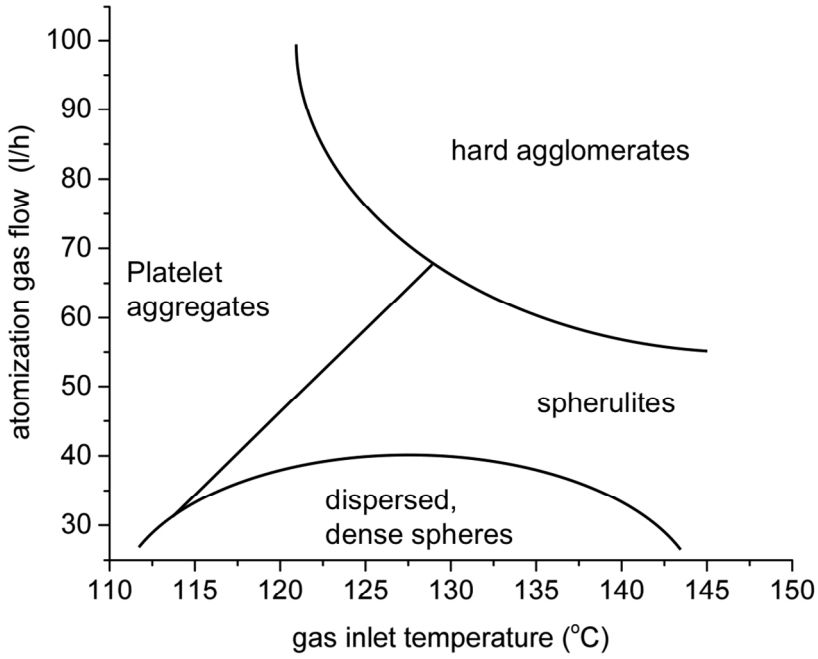

Fig. 7. A processing map for a concentration of 8.66g/100 ml and a solution feed rate of 21 ml/min shows morphology regions.
123x95mm (300 x 300 DPI)

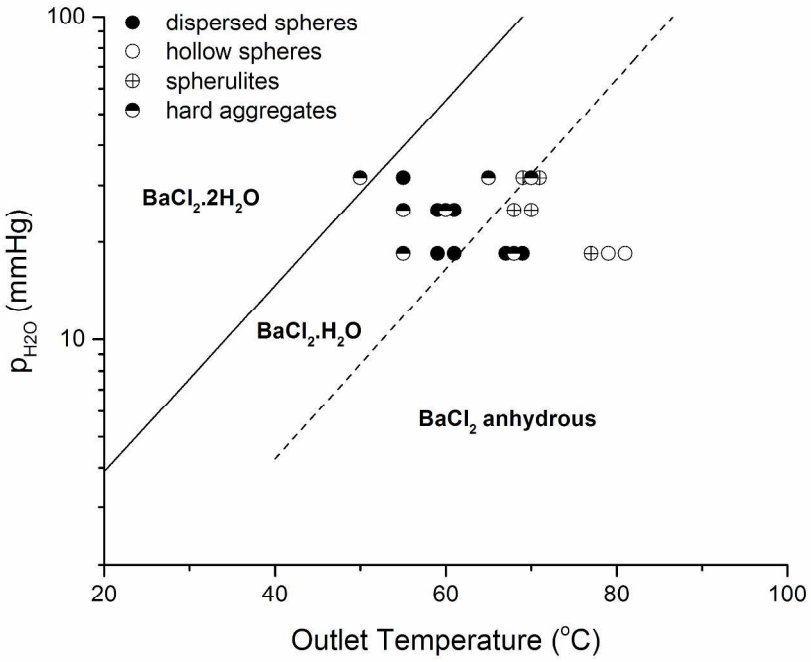

Fig. 8. The water vapor pressure above solid BaCl2□nH2O at the outlet is calculated for a representative set of spray drying samples. The solid line represents equilibrium vapor pressure between the mono-hydrate and di-hydrate phases, while the dotted line represents the equilibrium vapor pressure between the anhydrous and mono-hydrate phases38.
269x205mm (300 x 300 DPI)

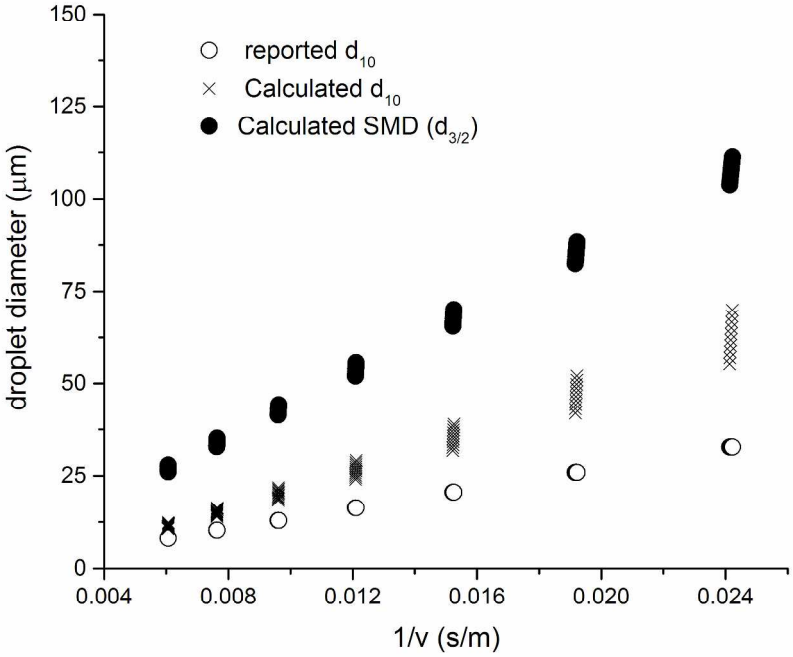

Fig. 9 The calculated d3,2 plotted versus the inverse relative gas-solution velocity is slightly higher than both the arithmetic average droplet size reported in the spray-dryer literature and the arithmetic average droplet size calculated by the Kim-Marshall equation.
279x215mm (300 x 300 DPI)

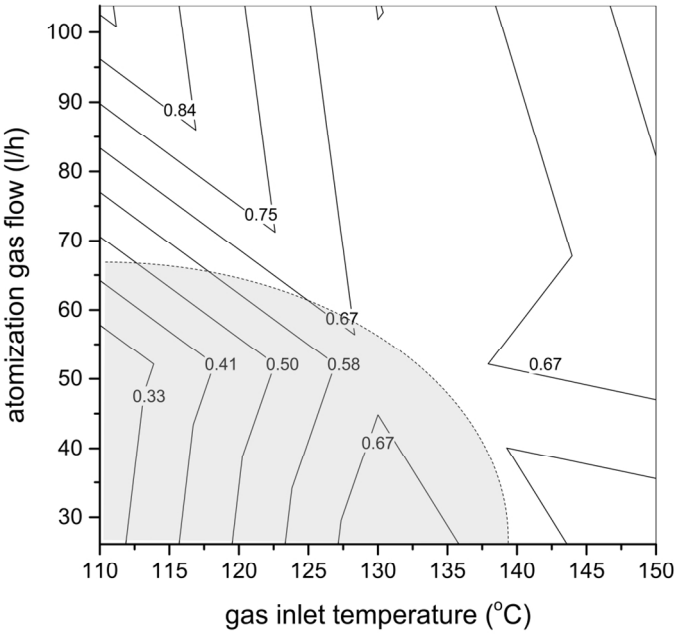

Fig. 10. A contour map of Peclet number versus gas inlet temperature and gas flow for a pump rate of 12 ml/min and feed solution concentration of 8.66 g/100 ml shows good agreement with the experimental morphology boundary (grey shaded region) for higher density, dispersed aggregates.
125x93mm (300 x 300 DPI)